Near-Unity Nitrate to Ammonia conversion via reactant enrichment at the solid-liquid interface

Wanru Liao[1,2,9], Jun Wang[1,2,9], Yao Tan[1], Xin Zi[1], Changxu Liu [ID][3], Qiyou Wang[1], Li Zhu[4], Cheng-Wei Kao[5], Ting-Shan Chan [ID][5], Hongmei Li[1], Yali Zhang[6], Kang Liu[1], Chao Cai [ID][1], Junwei Fu [ID][1], Beidou Xi [ID][7] ✉, Emiliano Cortés [ID][4] ✉, Liyuan Chai[8] & Min Liu [ID][1,8] ✉

Electroreduction of nitrate (NO_3^-) to ammonia (NH_3) is a promising approach for addressing energy challenges. However, the activity is limited by NO_3^- mass transfer, particularly at reduction potential, where an abundance of electrons on the cathode surface repels NO_3^- from the inner Helmholtz plane (IHP). This constraint becomes pronounced as NO_3^- concentration decreases, impeding practical applications in the conversion of NO_3^--to-NH_3. Herein, we propose a generic strategy of catalyst bandstructure engineering for the enrichment of negatively charged ions through solid-liquid (S-L) junction-mediated charge rearrangement within IHP. Specifically, during NO_3^- reduction, the formation of S-L junction induces hole transfer from Ag-doped MoS_2 (Ag-MoS_2) to electrode/electrolyte interface, triggering abundant positive charges on the IHP to attract NO_3^-. Thus, Ag-MoS_2 exhibits a ~ 28.6-fold NO_3^- concentration in the IHP than the counterpart without junction, and achieves near-100% NH_3 Faradaic efficiency with an NH_3 yield rate of ~20 mg h^{-1} cm^{-2} under ultralow NO_3^- concentrations.

Ammonia (NH_3), one of the most common industrial chemicals, is crucial for the production of agricultural fertilizers and holds immense potential as a green hydrogen-rich fuel[1–3]. The current global ammonia demand exceeds 180 million tons annually, primarily fulfilled through industrial-scale production of energy-intensive Haber-Bosch (H-B) process[1,4]. Within this process, steam-reformed hydrogen (H_2) undergoes reaction with nitrogen (N_2) under elevated temperature (~500 °C) and pressure (>100 atm)[5,6], which not only accounts for approximately 1.4% of global carbon dioxide (CO_2) emissions, but also necessitates the

consumption of 2% of the world's total energy supply[7,8]. Recently, electrocatalytic methodologies have surfaced as a viable clean energy pathway for decentralized ammonia synthesis at room temperature, accommodating a range of infrastructure scales and potentially powered by locally sourced renewable energy sources[9,10]. Despite the substantial global demand that may sustain the traditional ammonia production route in the near future, the electrochemical ammonia synthesis can be promising complementary process to the Haber–Bosch technology for contributing to decarbonizing ammonia production[11,12].

[1]Hunan Joint International Research Center for Carbon Dioxide Resource Utilization, State Key Laboratory of Powder Metallurgy, School of Physics, Central South University, Changsha 410083 Hunan, P. R. China. [2]School of Chemistry and Pharmaceutical Engineering, Changsha University of Science and Technology, Changsha, Hunan, P. R. China. [3]Centre for Metamaterial Research & Innovation, Department of Engineering, University of Exeter, Exeter, UK. [4]Nanoinstitut München, Fakultät für Physik, Ludwig-Maximilians-Universität München, München, Germany. [5]National Synchrotron Radiation Research Center, Hsinchu, Taiwan. [6]Key Laboratory of Land Surface Pattern and Simulation, Institute of Geographic Sciences and Natural Resources Research, Chinese Academy of Sciences, Beijing, P. R. China. [7]State Key Laboratory of Environmental Criteria and Risk Assessment, Chinese Research Academy of Environmental Sciences, Beijing, P. R. China. [8]School of Metallurgy and Environment, Central South University, Changsha, P. R. China. [9]These authors contributed equally: Wanru Liao, Jun Wang. ✉e-mail: xibd@craes.org.cn; Emiliano.Cortes@lmu.de; minliu@csu.edu.cn

Recently, diverse electrochemical approaches have been explored to address the varied demands for NH_3 production in the future energy landscape, encompassing the electrochemical N_2 reduction reaction (NRR)[13–15], lithium-mediated NRR[16–19] and nitrate reduction reaction (NO_3RR)[20–22]. Among them, the present NH_3 yield via NO_3RR surpasses those of NRR by two to three orders of magnitude, mainly due to the relatively lower dissociation energy of the N=O bond (204 kJ mol^{-1}) of nitrate anion (NO_3^-) compared to the N≡N bond (941 kJ mol^{-1})[23,24]. Besides, NO_3^- exhibits a ubiquitous presence within contaminated groundwater and industrial effluent[25,26], with their availability further augmented through the oxidation process of atmospheric N_2 as the source of nitrogen[9,27,28]. Consequently, the NO_3RR pathway has emerged as one of the most potential in renewable NH_3 production.

While continuous progress has been made in NO_3RR under high NO_3^- concentrations (>100 mM)[11,29–31], achieving large throughput and effective NO_3^- reduction in groundwater with concentrations below 10 mM remains a challenge, presenting a limited NH_3 yield rate below 5 mg h^{-1} cm^{-2} and a Faradaic efficiency (FE) below 85%[22,32–34]. On the other hand, a considerable portion of the groundwater, stemming from both agricultural and industrial sources[35–40], has a diluted concentration, necessitating a platform suitable for operation at low concentration. More importantly, the removal process of NO_3^- continuously reduces its concentration, inevitably reaching the low concentration regime with reduced performance.

To mitigate the degradation in low concentration, significant efforts have been devoted to concentrating NO_3^- locally around electrodes, employing various strategies such as porous carbon framework encapsulation[32], built-in electric field regulation[41], and nitrogen-vacancy engineering[42]. However, these endeavors primarily focus on manipulating catalyst properties for NO_3^- enrichment, with limited exploration of interfacial NO_3^- transfer under operational conditions. Particularly, at the reduction potential, an excess of electrons accumulates on the cathode surface, leading to a repulsion of negatively charged NO_3^- ions from the inner Helmholtz plane (IHP), where the catalytic reactions occur[27]. This ubiquitous effect of charge repulsion hinders the mass transfer and sets up an intrinsic bottleneck for the catalytic process.

Here, we overcome the fundamental limitation through utilizing a solid-liquid (S-L) junction[43,44] to manipulate the charge distribution within the IHP region. By employing proper bandstructure engineering of the catalyst (p-type Ag-doped MoS_2, Ag-MoS_2), the enhanced interfacial charge transfer endows reinforced S-L junction to facilitate the NO_3^- enrichment in IHP (Fig. 1), showcasing a ~27.6-fold increase in NO_3^- concentration compared to the counterpart without junction. As a proof of concept, the Ag-MoS_2 platform demonstrates impressive performance, including a record-high NH_3 yield rate of ~20 mg h^{-1} cm^{-2} and NH_3 FE of ~100%, outperforming previous results obtained under low NO_3^- levels[22,32,34,36]. Furthermore, the high NO_3^--to-NH_3 conversion efficiency (99.3%) enables the removal of nitrate from 100 mM to low levels of 0.54 mM within 3 h, in sharp contrast with the reference (still relatively high level under 48 h operation). Notably, we successfully convert NO_3^- into high-purity NH_4Cl products with near-unity efficiency by coupling the NO_3RR with an air stripping process, demonstrating the potential of large throughput ammonia production in a sustainable way.

Results

Based on the merits of appropriate band gap (1.2–1.9 eV), excellent conductivity, adjustable Fermi level position, and two-dimensional characteristics of large specific surface area, MoS_2 was selected as the platform for the electrocatalysis, with intentionally doped Ag as the enabler for the desired S-L junction formation. The Ag-doped MoS_2 (Ag-MoS_2) catalyst was grown in situ on a carbon cloth using a one-step hydrothermal method (Supplementary Fig. 1, see "Methods"). MoS_2 as a reference was synthesized through a similar route, excluding the addition of a silver source. Scanning electron microscopy (SEM), transmission electron microscopy (TEM), and high-resolution TEM (HRTEM) revealed a nanoflower morphology of Ag-MoS_2 with (100) crystal plane orientation (Fig. 2a–c and Supplementary Fig. 2), maintaining a morphology similar to that of MoS_2 (Supplementary Figs. 3, 4). Energy-dispersive X-ray (EDX) elemental mapping illustrated the uniform distribution of Ag species on MoS_2 nanoflowers (Fig. 2d). The X-ray diffraction (XRD) patterns of Ag-MoS_2 and MoS_2 were similar, indicating no formation of secondary phases after Ag doping (Fig. 2e). Inductively coupled plasma optical emission spectrometry (ICP-OES) determined the optimal Ag content in Ag-MoS_2 to be 3.49 wt% (Supplementary Table 1).

To analyze the surface chemical states of the catalysts, high-resolution X-ray photoelectron spectroscopy (XPS) was performed
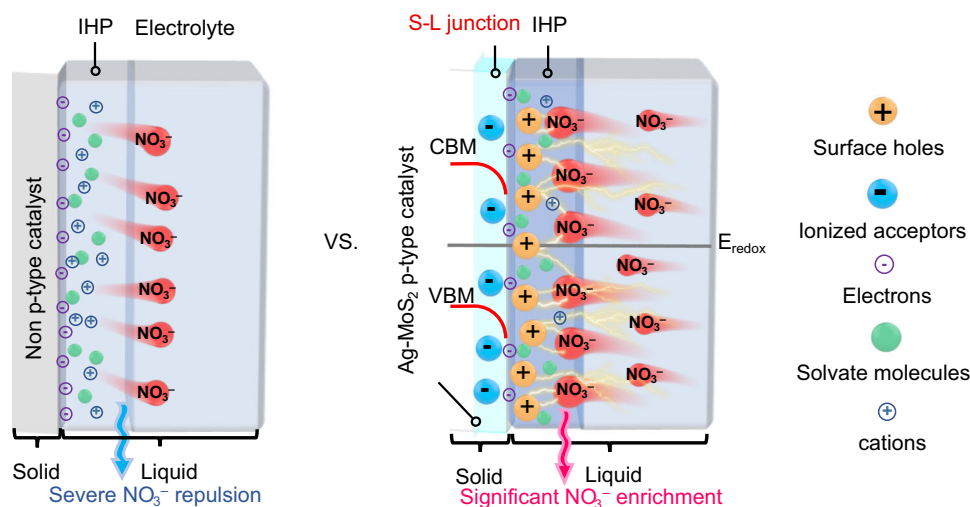
Fig. 1 | Solid-liquid (S-L) junction-mediated charge rearrangement to attract NO_3^-. Schematic diagram of S-L junction-mediated NO_3^- enrichment within the IHP region over Ag-MoS_2 at the reduction potential. E_{redox} represents the theoretical redox potential of NO_3^-/NH_3. CBM and VBM express the conduction band minimum and valence band maximum of Ag-MoS_2, respectively. Note: IHP contains surface holes, solvate molecules, and NO_3^- anions and cations. Electrons accumulate on the electrode surface under negative polarization. Ionized acceptors exist in the S-L junction (see detailed discussions in the supplementary discussions).
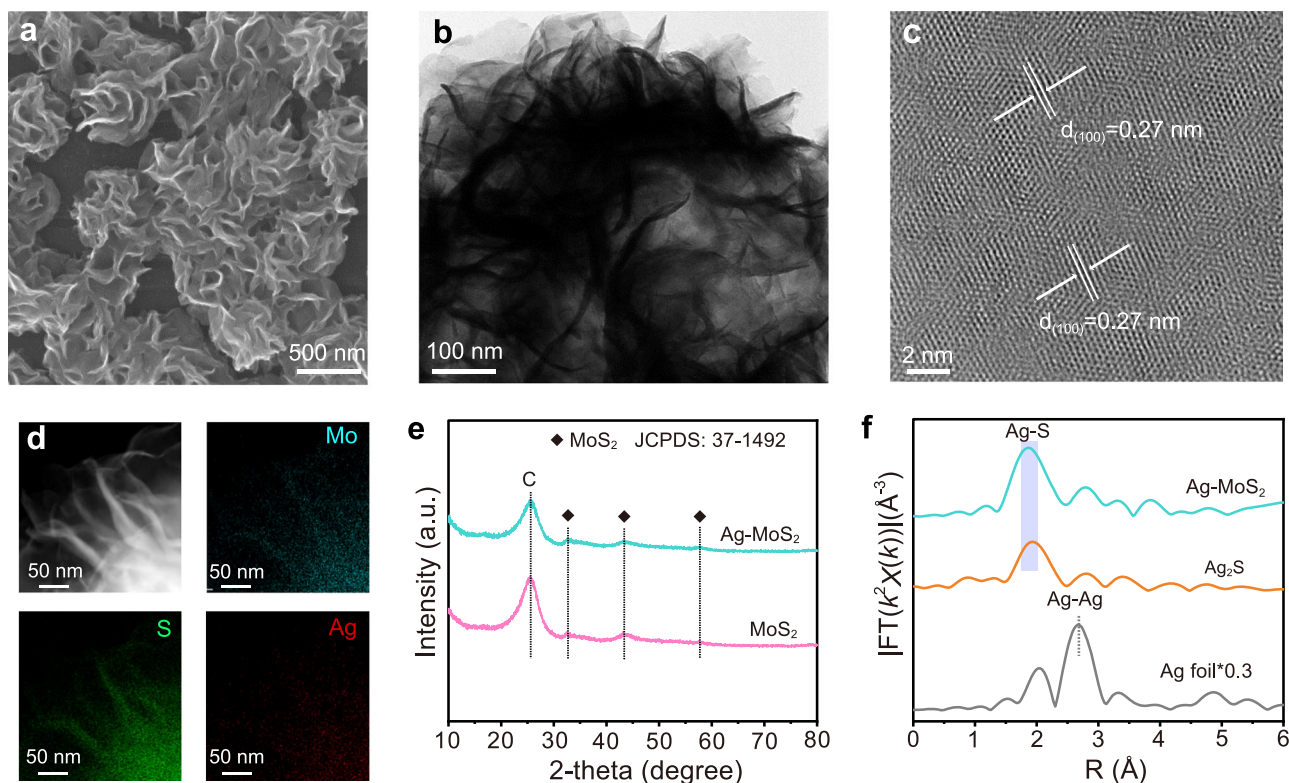
Fig. 2 | Synthesis and structural characterizations of Ag-MoS₂. a SEM, (**b**) TEM, (**c**) HRTEM, and (**d**) EDX mapping of Ag-MoS₂. **e** XRD patterns of Ag-MoS₂ and MoS₂. **f** Fourier transformed k^2-weighted EXAFS spectra of Ag-MoS₂ and reference samples.

(Supplementary Fig. 5). The Mo $3d$ and S $2p$ XPS spectra indicated the presence of Mo^{4+} and S^{2-} in both Ag-MoS₂ and MoS₂[45,46]. In the Ag $3d$ spectra, characteristic peaks at 368.16 and 374.13 eV were assigned to the Ag-S bond[47,48]. To further elucidate the coordination structure of Ag species, X-ray absorption fine structure (XAFS) was investigated. The Mo K-edge X-ray absorption near edge structure (XANES) spectra exhibited a higher pre-edge absorption energy of Ag-MoS₂ than those of Mo foil and MoS₂ (Supplementary Fig. 6a), implying that the doping Ag species induced decreased electron density on the Mo site. From the Ag K-edge XANES spectra, the absorption energy of Ag-MoS₂ located between those of Ag foil and Ag₂S references (Supplementary Fig. 6b), indicating the valence state of the doped Ag within 0 to 1. The Fourier-transformed extended XAFS (EXAFS) of Ag-MoS₂ exhibited characteristic peaks of the Ag-S bond at 1.9 Å, confirming the coordination of Ag with S atoms (Fig. 2f). These comprehensive results provide clear evidence of the synthesis of Ag-doped MoS₂ catalysts.

To investigate the construction and regulation of the solid-liquid (S-L) junction, we conducted ultraviolet photoelectron spectra (UPS) and Mott-Schottky (M-S) measurements. The UPS results (Supplementary Fig. 7) demonstrated a significant increase in the work function of Ag-MoS₂ (5.47 eV) compared to MoS₂ (4.98 eV), indicating a downward-shifted Fermi level after Ag doping. In addition to the UPS method, KPFM measurements were carried out to collaboratively demonstrative the increase of work function by Ag doping (Supplementary Figs. 8, 9)[49]. The surface potential difference between Ag-MoS₂ and FTO substrate was ~ 230 mV, while 20 mV for MoS₂. Correspondingly, the work functions of Ag-MoS₂ and MoS₂ were 5.13 and 4.92 eV, respectively. The variation trend was in consistent with UPS results, indicating a relatively high work function of Ag-MoS₂. M-S plots further revealed the Fermi level potential (E_F) of Ag-MoS₂ (1.07 V *versus* RHE) and MoS₂ (0.53 V *versus* RHE), respectively (Fig. 3a), surpassing the theoretical redox potential of NO_3^-/NH_3 (E_{redox}, 0.27 V *versus* RHE under neutral conditions (pH 6.71))[50–53]. The calculated carrier concentration of Ag-MoS₂ is 1.14×10^{19} cm⁻³, 1.8 times higher than that of

MoS₂ (6.3×10^{18} cm⁻³, Supplementary Table 2). Thus, the Ag dopant as the electron acceptor to increase the carrier concentration and work function of MoS₂ was verified.

Upon contact with the NO_3^--containing electrolyte, the potential difference between the E_F and the E_{redox} (E_F-E_{redox}) triggered charge transfer between the catalyst surface and the inner Helmholtz plane (IHP), forming positively charged IHP on the electrolyte side (Supplementary Fig. 10). Specifically, p-type MoS₂ catalysts exhibited the characteristic of hole conduction. Under the drive of E_F-E_{redox}, the holes (majority carrier) in the valance band would transfer from the semiconductor surface to the electrolyte, inducing charge rearrangement within the IHP region (Supplementary Fig. 10a)[54]. Meanwhile, the high carrier concentration (1.14×10^{19} cm⁻³) and thin space charge layer width (5.88 nm) of Ag-MoS₂ can contribute to the increase of probability for hole tunneling effect (Supplementary Fig. 10b and Supplementary Tables 2, 3), which benefited positive charges distribution within IHP. Compared to MoS₂ with a limited E_F-E_{redox} (0.23 V), the larger E_F-E_{redox} value of Ag-MoS₂ (0.76 V) provoked 0.53 V more downward band bending, intensifying the built-in electric fields at S-L junctions (see detailed quantitative methods and discussion in Supplementary Figs. 11–13).

To explore the influence of S-L junction on the charge distribution within the IHP region, alternating current voltammetry (ACV) measurements were employed (Fig. 3b)[55,56]. ACV was a non-destructive technique which had been widely utilized to record the adsorption behavior change in the IHP range[57,58]. Compared to MoS₂, Ag-MoS₂ exhibited a negatively shifted potential of zero charges (PZC, 0.57 V *versus* RHE). PZC was adopted as an indicator for the IHP structure evolution, and the negative PZC indicated the adsorption of anion on the IHP region of Ag-MoS₂ (Fig. 4 and Supplementary Figs. 14, 15)[59,60]. To investigate the charge distribution under reduction potential, surface capacitance (charge distribution within the solid-liquid interface) of the catalysts was obtained from Nyquist plots at − 0.6 V *versus* RHE (Supplementary Fig. 16). The capacitance of Ag-MoS₂ (9.5 μC cm⁻²) was lower than that of
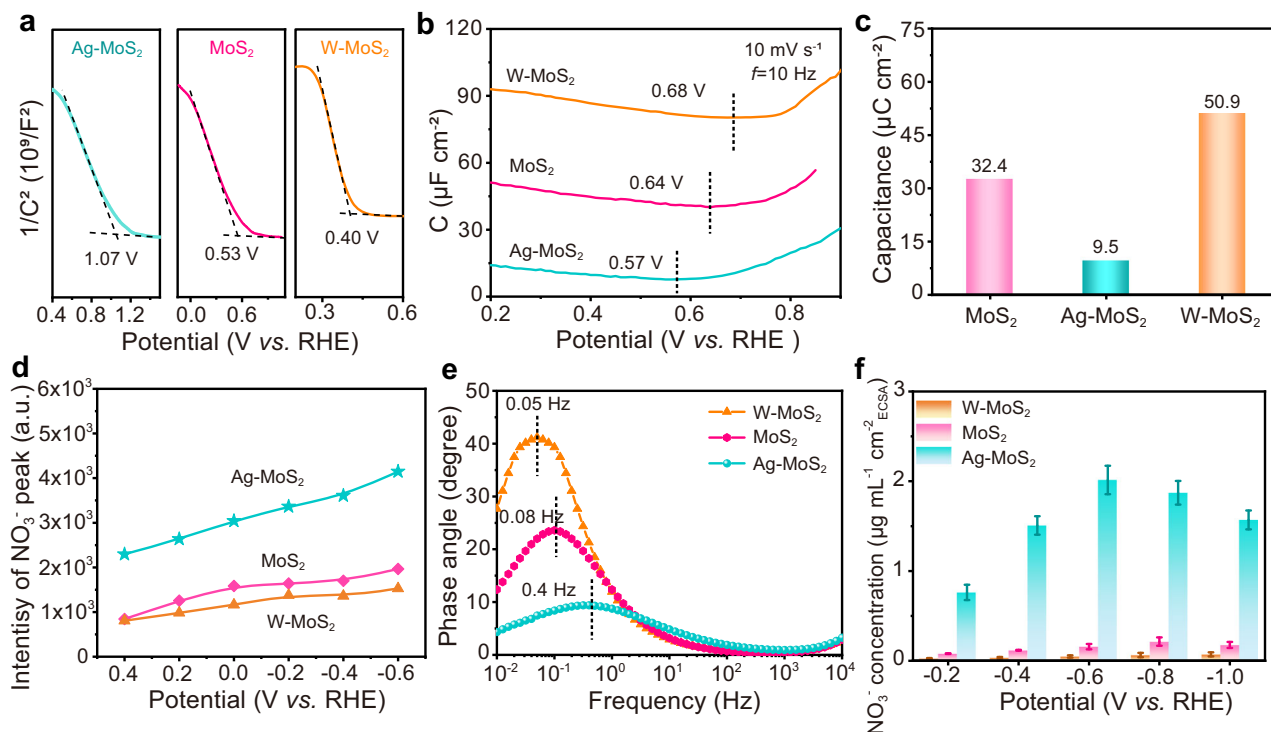
Fig. 3 | S-L junction-mediated NO_3^- enrichment within IHP region. a Mott-Schottky plots of Ag-MoS$_2$, MoS$_2$, and W-MoS$_2$ catalysts. **b** The non-Faradaic capacitance-potential curves for the diverse catalysts. The potential of zero charge (PZC) describes the condition when the capacitance on a surface is minimal. **c** The fitted surface capacitance of the three catalysts. **d** The peak intensity of absorbed NO_3^- from in situ Raman spectra of catalysts at various potentials. **e** Bode plots of catalysts at the reduction potential of − 0.6 V versus RHE in 10 mM NO_3^- electrolyte. **f** The ECSA normalized NO_3^- adsorption capacity at different applied potentials on catalysts.
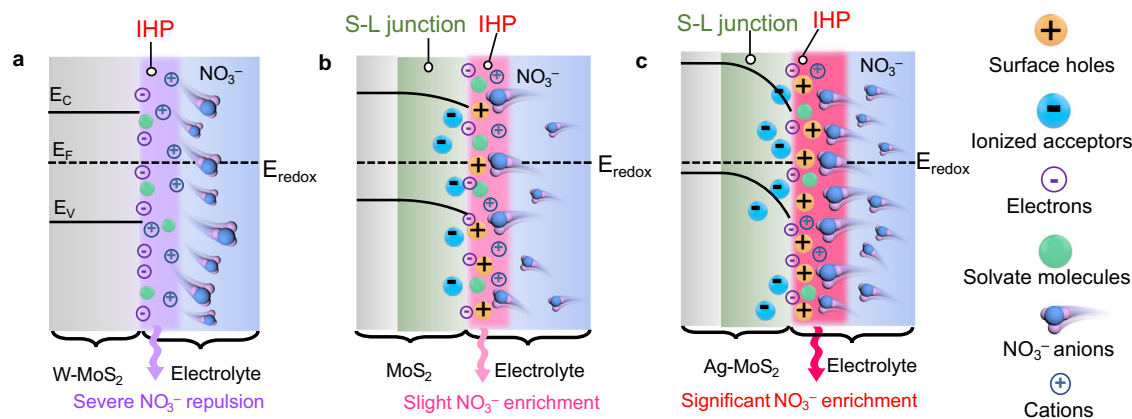
Fig. 4 | NO_3^- distribution on IHP region over MoS$_2$-based catalysts. a W-MoS$_2$ without S-L junction, (**b**) MoS$_2$ with weak S-L junction, and (**c**) Ag-MoS$_2$ with strong S-L junction at the reduction potential.

MoS$_2$ (32.4 μC cm^{-2}), indicating significant positive charges distribution of Ag-MoS$_2$ (Fig. 3c). High valence metals had been reported to serve as electron donors to regulate the E_F away from VBM, for enhancing the n-type characteristics of semiconductors[61]. Thus, we also prepared the reference samples with tungsten (W) doping, to demonstrate the effect of the S-L junction. In contrast, a n-type W-doped MoS$_2$ (W-MoS$_2$) counterpart with no obvious S-L junction (Fig. 3a and Supplementary Figs. 7 and 17–21) had higher PZC value (0.67 versus RHE, Fig. 3b) and capacitance (50.9 μC cm^{-2}, Fig. 3c), suggesting extensive anions packed on its IHP. These results confirmed that Ag doping can effectively enhance the built-in electric field at the S-L junction, which consequently induced abundant positive charges distributed on the IHP of Ag-MoS$_2$ at the reduction potential.

To investigate the S-L junction-mediated NO_3^- enrichment effect, in situ Raman spectra of the three catalysts were carried out (Supplementary Fig. 22). Apart from the observed H$_2$O peak (at 1605 cm^{-1})[62–64], the NO_3^- peak (at 1046 cm^{-1})[65,66] was detected at the potentials from open circuit potential (OCP) to − 0.6 V versus RHE, indicating NO_3^- adsorption near the catalyst surface. Notably, Ag-MoS$_2$ with a stronger NO_3^- peak than those of MoS$_2$ and W-MoS$_2$ at each reduction potential (Fig. 3d) demonstrated a pronounced NO_3^- enrichment effect. In Bode phase plots (Fig. 3e), compared with W-MoS$_2$ (0.05 Hz) and MoS$_2$ (0.08 Hz), the higher frequency of Ag-MoS$_2$ (0.4 Hz) implied a facilitated interfacial charge transfer process, which can be ascribed to its intensified NO_3^- accumulation within the IHP region[67,68]. Elemental mapping displayed obvious N and O signals on Ag-MoS$_2$ nanoflowers

during the electrolysis of −0.6 V *versus* RHE in NO_3^--contained electrolyte, whereas they were relatively shallow or inconspicuous on MoS_2 and $W-MoS_2$ (Supplementary Figs. 23–25), disclosing a large number of NO_3^- migrated to the surface.

To quantify the NO_3^- concentration, the NO_3^- enrichment capacity of the three catalysts was measured by ion chromatography (IC) at applied potentials (Fig. 3f and Supplementary Fig. 26, see "Methods"[69]). By normalizing the NO_3^- adsorption capacity with respect to the electrochemical active surface area (ECSA), the concentration of NO_3^- adsorbed on $Ag-MoS_2$ presented a normal distribution trend as the potential ranging from − 0.2 to −1.0 V *versus* RHE (Fig. 3f and Supplementary Fig. 27), and reached the peak at − 0.6 V *versus* RHE (2.0 µg mL^{-1} cm$^{-2}_{ECSA}$). Due to the different Fermi level position, the adsorbed NO_3^- concentration of MoS_2 and $W-MoS_2$ peaked at more negative potentials of − 0.8 and −1.0 V *versus* RHE, respectively. As the Ag dopant acted as the electron acceptor to increase the carrier concentration (Supplementary Table 2), it induced an intensified surface band bending when the $Ag-MoS_2$ was contacted with the NO_3^- contained electrolyte. Thus, the maximum adsorbed NO_3^- concentration of $Ag-MoS_2$ surpassed MoS_2 and $W-MoS_2$ by factors of 8.8 and 27.6, respectively, at their optimal adsorption potentials. The NO_3^- adsorption concentration was also normalized by specific surface area (SSA), this trend aligned with the ECSA normalization results (Supplementary Fig. 28), highlighting superior intrinsic NO_3^- adsorption capability of $Ag-MoS_2$. The lowest surface capacitance at −0.6 V *versus* RHE suggested massive positive charges within IHP (Supplementary Fig. 29), contributing to the peaked NO_3^- concentration at that potential. While the excessive potential (above −0.6 V) triggered severe downward shift of E_F into the valence band of $Ag-MoS_2$ (Supplementary Fig. 30 and Supplementary Table 4, see details in the corresponding discussion), forming a degenerate semiconductor with metallic property, as proved by the decreased arc radius at high-frequency region. This could severely destroy the S-L junction to impact the enrichment of NO_3^-. We also implemented finite element method simulations for the NO_3^- distribution on the three catalyst surfaces through COMSOL, which matched the experimental results demonstrated (Supplementary Fig. 31 and Supplementary Table 5).

Under the S-L junction-induced NO_3^- enrichment feedback, we evaluated the NO_3RR performance in a standard three-electrode system at ambient temperature and pressure. In this reaction system, NH_4^+, NO_3^-, and NO_2^- were monitored and quantified by coloration and ^1H nuclear magnetic resonance (NMR) spectroscopy[70] (Supplementary Figs. 32–35). A typical industrial and agricultural groundwater-relevant NO_3^- concentration of 10 mM was reasonably used in the electrolyte for the standard electrochemical tests[35,37,38,69]. Linear sweep voltammetry (Supplementary Fig. 36) curves of $W-MoS_2$, MoS_2, and $Ag-MoS_2$ all presented a higher current density between −0.5 and − 1.65 V *versus* RHE in the NO_3^- electrolyte relative to NO_3^--free solutions. Particularly, the most significant current difference occurred on $Ag-MoS_2$, revealing its promising NO_3RR activity.

Following the chronoamperometry measurements at various applied potentials tested in a flow cell reactor (Supplementary Fig. 37), the NO_3RR performance was assessed for the three catalysts with a 0.5 h duration. Of these, $Ag-MoS_2$ displayed the superior performance (Fig. 5a, b), with a near unit NH_3 Faradaic efficiency (FE) of 99.7% at − 0.6 V *versus* RHE (~ 200 mA cm^{-2}) and an optimal NH_3 yield rate of 20.1 mg h^{-1} cm^{-2} at −1.0 V *versus* RHE (~ 340 mA cm^{-2}). The optimal NH_3 yield rate value was about 3.4-folds and 1.7-folds than those of $W-MoS_2$ and MoS_2, respectively. Similarly, the peak NH_3 FE of $Ag-MoS_2$ was approximately 3.2-folds and 1.8-folds than those of $W-MoS_2$ and MoS_2, respectively. These results displayed the superior NO_3RR performance of $Ag-MoS_2$ compared to its counterparts. Moreover, the performance surpassed most state-of-the-art NH_3 activity ever reported at a low NO_3^- system (Fig. 5c and Supplementary Table 6)[22,32,34,71,72]. The electrochemically active surface area-normalized NH_3 yield rate also

clarified the excellent intrinsic activity of $Ag-MoS_2$ (Supplementary Figs. 27 and 38). The blank experiments without adding NO_3^- to the electrolyte or working at OCP produced a negligible amount of NH_3 (Supplementary Fig. 39), excluding the possible interference on the quantification results. Besides, the possible contribution of Ag nanoparticles on the NO_3^- enrichment and NO_3RR performance of MoS_2 has been eliminated (Supplementary Figs. 40–43).

To reveal the significance of NO_3^- enrichment for superior NO_3RR performance under a low-NO_3^- concentration system, EIS measurements were conducted (Fig. 5d and Supplementary Fig. 16). In the Nyquist plots, semicircles with similar radii at the high-frequency region of the three samples indicated nearly equivalent conductivity. At the low-frequency region, $W-MoS_2$ without S-L junction showed a straight line with a slope of 45°, suggesting that NO_3^- mass transfer was the rate control step for NO_3RR. In contrast, the smaller arc radius over $Ag-MoS_2$ illustrated the enhanced reaction rate of NO_3RR (from 16.41 to 6.92 Ω cm^{-2}, Supplementary Table 7). The lowest phase angle of $Ag-MoS_2$ in bode plots also testified its accelerated catalytic kinetics, ascribing to the distinct NO_3^- enrichment effect (Fig. 3e). In addition, from the NO_3RR performance at a wide range of NO_3^- concentrations (Supplementary Fig. 44), the optimal $Ag-MoS_2$ in K_2SO_4 system (Supplementary Figs. 45–46) exhibited its broad adaptability and achieved an excellent NH_3 FE at − 0.6 V *versus* RHE (> 90%, in Supplementary Fig. 47), even at ultra-low concentration (1 mM). While the NH_3 yield rate of $Ag-MoS_2$ was significantly higher than those of $W-MoS_2$ and MoS_2 in low NO_3^- concentration (Supplementary Fig. 44, insert), it gradually became comparable as the concentration increased. These results highlighted the importance of NO_3^- enrichment to overcome the constraint of low-concentration NO_3^- electroreduction to NH_3, via the S-L junction-mediated effect.

To examine the NO_3^- removal capability of $Ag-MoS_2$, the conversion tests with an initial 100 mM NO_3^- were carried out in an H-cell reactor, and the remaining products were measured. Impressively, the NO_3RR on the three samples followed typical quasi-first-order kinetics, and the NO_3^- to NH_3 selectivity of $Ag-MoS_2$ was up to 99.3% within only 3 h of electrolysis at − 0.6 V versus RHE (NO_3^- concentration decreased sharply from 100 mM to 0.54 mM, Fig. 5e and Supplementary Fig. 48), manifesting that nearly all the N sources were converted into NH_3 (Supplementary Fig. 49). Comparatively, the NO_3^- to NH_3 conversion efficiency of $W-MoS_2$ and MoS_2 were as low as ~16% and ~ 30%, and the residual NO_3^- still remained a relatively high level of 4.64 mM and 11.78 mM even after 48 h (Supplementary Fig. 50). Also, $Ag-MoS_2$ behaved with stable performance and robust structure, as demonstrated by the steady eight-cycling NO_3RR process at 25 °C (Fig. 5f), the negligible morphology change, tiny phase structure difference, and slight chemical valence state shift after the electrolysis (Supplementary Figs. 51, 52).

Furthermore, we demonstrated the practicality of the proposed setup for efficient NH_3 collection. Here, we integrated electrocatalysis with an air-stripping method for the recovery of high-purity ammonia products at − 1.0 V *versus* RHE (Fig. 5g). After the NO_3RR process, the cathodic electrolyte was transferred to a conical flask and adjusted to an alkaline state. Due to the high NH_3 vapor pressure under alkaline conditions, the produced NH_3 was efficiently extracted at 70 °C using an air stripping method (see details in Methods)[73,74]. Consequently, approximately 98.9% of the NH_3 vapor was successfully stripped out from the electrolyte (Fig. 5h), indicating favorable NO_3^- conversion and simultaneous high-efficiency NH_3 generation. Subsequently, around 97.3% of the outflowing NH_3 gas was collected in an HCl solution, and approximately 97.1% of NH_4Cl powder was finally obtained after rotary evaporation. The high-purity NH_4Cl products were confirmed by XRD measurement (Supplementary Fig. 53), highlighting their potential as fertilizer for agricultural production.

Next, to investigate the practical application prospect, complex electrolyte (which included CO_3^{2-}, Na^+, Cl^-, K^+, NO_3^-, and SO_4^{2-}) was prepared to simulate the nitrate-containing wastewater condition[75].
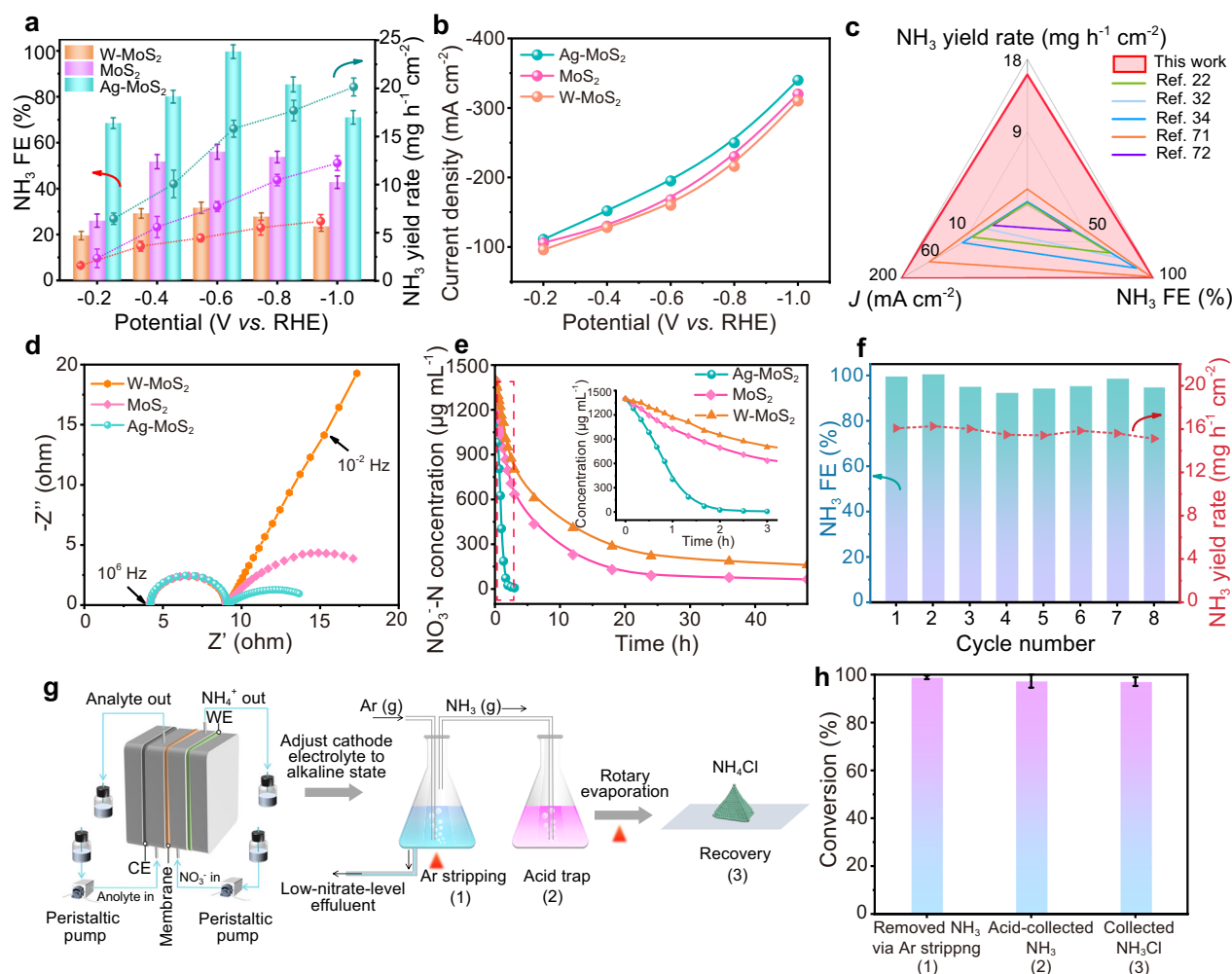
Fig. 5 | NO₃RR performance under ultralow NO₃⁻ concentrations. a NH₃ yield rate and NH₃ FE of catalysts in 10 mM NO₃⁻ electrolyte at various applied potentials. **b** *I–V* plots of catalysts in 0.5 M K₂SO₄ with 10 mM NO₃⁻ electrolyte at various potentials for 0.5 h electrolysis. **c** A summary of recent NO₃RR works on NH₃ yield rate, NH₃ FE and current density under ultralow NO₃⁻ concentrations (NO₃⁻ concentration ≤ 10 mM)[22,32,34,71,72]. **d** EIS tested at −0.6 V versus RHE in 10 mM NO₃⁻ electrolyte. **e** NO₃⁻ removal in initial 0.5 M K₂SO₄ with 100 mM NO₃⁻ electrolyte at −0.6 V versus RHE in H-cell reactor. After 3 h of electrolysis, only 0.54 mM of

NO₃⁻−N. Insert was the enlarged vision within 3 h. **f** NO₃RR performance stability over Ag-MoS₂ measured in a 0.5 M K₂SO₄ with 10 mM NO₃⁻ electrolyte at −0.6 V versus RHE. **g** Schematic of the ammonia product synthesis process from 100 mM NO₃⁻ electrolyte to NH₄Cl at −1.0 V versus RHE. **h** The conversion efficiency of different steps for the ammonia product synthesis process. Numbers on the *x*-axis indicated the corresponding conversion steps in panel (g). Error bars indicate the relative standard deviations of the mean (*n* = 3).

The NH₃ Faradaic efficiency over Ag-MoS₂ in simulated wastewater was 76.7%, while the NH₃ yield rate reached 16.02 mg h⁻¹ cm⁻² (Supplementary Fig. 54a). The decreased NO₃RR performance can be ascribed to the presence of interfering ions that influenced the targeted adsorption of NO₃⁻. Although the NO₃RR performance in wastewater decreased to a certain extent, the NH₃ yield rate and Faradaic maintained 80% and 76% of the optimal performance for simple electrolyte. In the recovery process, approximately 73.9% of NH₄Cl powder was finally obtained (Supplementary Fig. 54b). Also, we have evaluated the preparation cost of Ag-MoS₂ catalyst, whose price with 1 cm² was as low as 0.475 ¥ (Supplementary Table 8). These results suggested that the Ag-MoS₂ has the potential for the conversion of NO₃⁻ to ammonia product in actual industrial and agricultural wastewater.

To gain a deeper understanding of the NO₃RR mechanism over Ag-MoS₂ catalysts, we employed in situ attenuated total reflection infrared spectroscopy (ATR-IR) to capture intermediates and monitor the reaction. As the applied potential ranged from 0.4 to −1.0 V versus RHE (Fig. 6a), the detected NO₂ peaks (at ∼1530 cm⁻¹)[76] in the spectra of Ag-MoS₂ indicated the deoxygenation of NO₃⁻. The pronounced characteristic peaks of N-H (at 3200–3380 cm⁻¹)[77–79], -H (at ∼2050 cm⁻¹)[80], and

NH₄⁺ (at ∼1450 cm⁻¹)[81] verified the effective hydrogenation of nitrogen oxide intermediates to ammonia on a highly protonated surface. In comparison, the NO₂, -H, and NH₄⁺ signals were not prominent in the spectra of MoS₂ and W-MoS₂ (Supplementary Figs. 55, 56), indicating that the relatively slow reaction rates of the two catalysts resulted in less accumulation of related species on their surfaces. Online differential electrochemical mass spectrometry (DEMS) was further performed to detect molecular intermediates and products (Fig. 6b and Supplementary Figs. 57, 58). The mass-to-charge ratio (m/z) signals of NH₃ (17), H₂ (2), N₂ (28), NO (30), NH₂OH (33), and N₂O (44) were detected and tracked. Among the three catalysts, the NH₃ intensity was the strongest, while other signals (H₂, N₂, NO, and N₂O) shrunk over Ag-MoS₂, which demonstrated the promotion of NH₃ generation under the S-L junction-induced NO₃⁻ enrichment on the Ag-MoS₂ surface. Further, we calculated the electronic band structures and partial density of states (PDOS) through density functional theory (DFT). After Ag doping, the newly emerged band tail states at VBM extended the valence band of Ag-MoS₂ (Fig. 6c, d and Supplementary Fig. 59)[82,83], leading to the downward shift of the Fermi level. While, W doping induced upward shift of the Fermi level away from the VBM (Supplementary Fig. 60). These phenomena
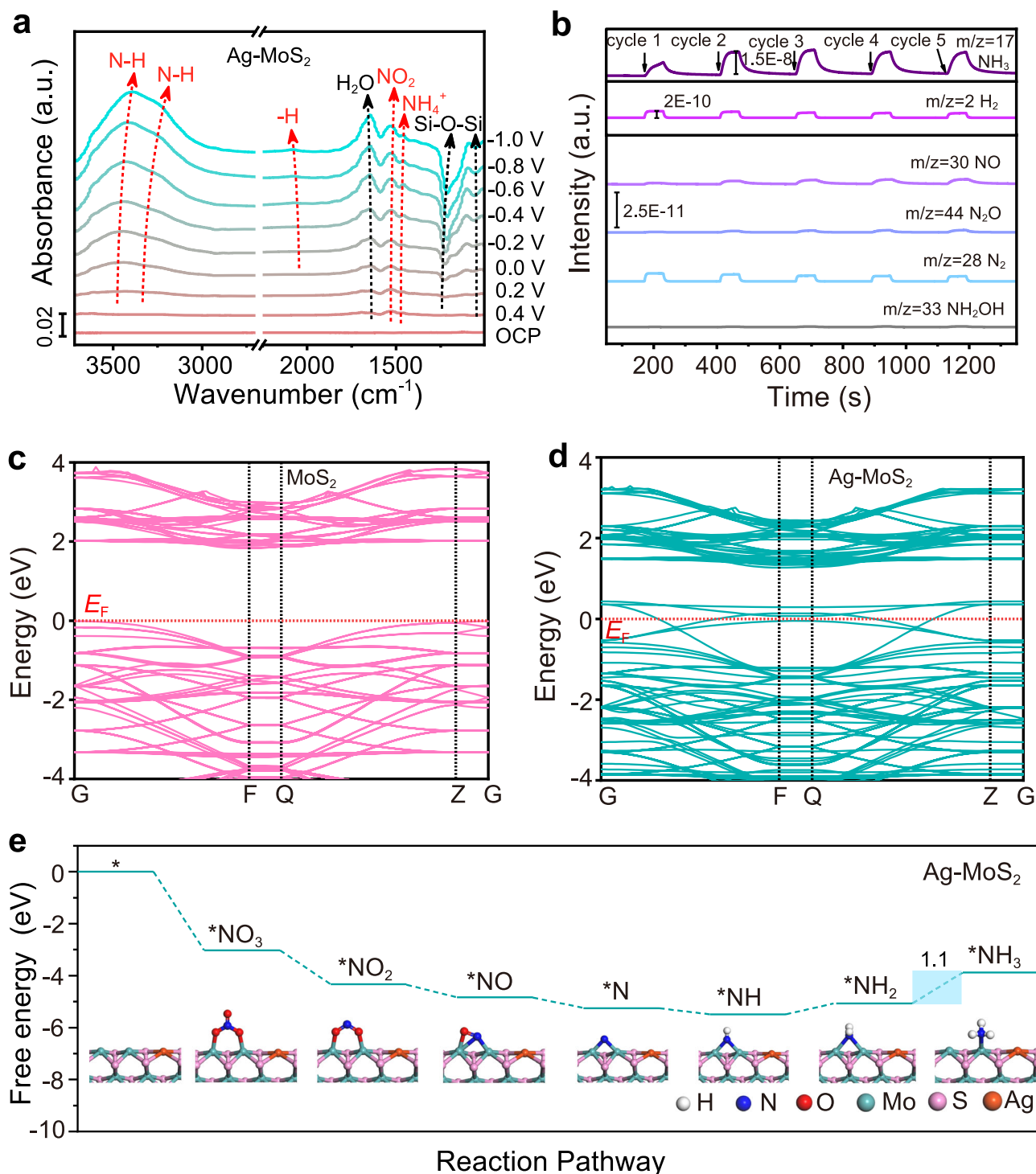
Fig. 6 | Mechanistic study on NO₃⁻ electroreduction. a In situ ATR-IR spectra of Ag-MoS₂. The Si-O signal was derived from the reduction of surface SiO₂ on the Si semi-cylindrical prism substrate under the applied potentials. **b** Online differential electrochemical mass spectrometry (DEMS) measurements of NO₃RR over Ag- MoS₂ under the potential of −0.6 V *versus* RHE. Electronic band structures of (**c**) MoS₂ and (**d**) Ag-MoS₂. **e** Gibbs free energy diagram of various intermediates generated during NO₃RR over Ag-MoS₂ at pH = 7.

were in consistent with UPS and M-S results, unveiling that Ag doping benefited the downward band bending within S-L junction and thus the charge transfer between IHP and the catalyst. The optimal reaction pathways of Ag-MoS₂ were also calculated (*NO₃ → *NO₂ → *NO → *N → *NH → *NH₂ → *NH₃) by comparing multiple possible branches (Fig. 6e and Supplementary Figs. 61–63). All three samples underwent the process of adsorption of NO₃⁻, deoxygenation of the N species, and hydrogenation of the N species to synthesize NH₃, in which the

*NH₂ → *NH₃ process was the potential-determining step (PDS). The Gibbs free energy change (ΔG) of this step was 1.1, 0.95, and 1.02 eV for Ag-MoS₂, MoS₂, and W-MoS₂ catalysts at pH = 7. The ΔG of Ag-MoS₂ was comparable to those of W-MoS₂ and MoS₂, suggesting that Ag doping had little contribution to the ΔG of PDS. Although MoS₂ and W-MoS₂ exhibited reduced ΔG of PDS at corresponding optimal NO₃⁻ adsorption potentials (Supplementary Figs. 61 and 64, 65), while, their NO₃RR performance were far below Ag-MoS₂ (Fig. 5a). These results further

indicated the decisive role of Ag doping-induced surface NO_3^- enrichment effect in promoting NO_3RR activity in low concentration system.

Discussion

In summary, we proposed a strategy to enrich charged chemicals in the vicinity o of the electrodes through catalyst bandstructure engineering, overcoming the bottleneck of mass transfer posed by intrinsic charge repulsion in electrocatalysis. We systematically demonstrated the S-L junction-mediated charge rearrangement effect on the IHP region, boosting electrocatalytic reduction of low-concentration NO_3^- to NH_3. COMSOL simulations and experimental measurements, including in situ Raman spectra, IC, EIS, and ACV, elucidated that the construction of S-L junction induced positively charged IHP, significantly enriching NO_3^- anions concentration (by a factor of 27.6) to break the mass transfer limitation at the reduction potential.

As a proof of concept, an optimized Ag-MoS_2 was introduced as a model platform for the NO_3RR flow cell system. We evaluated the comprehensive performance through the decontamination of nitrate polluted solution into drinkable level, which requires efficient catalytic process within a broad range of concentration and high conversion rate. By virtue of the unparalleled performance at ultra-low concentrations (~ 20 mg h^{-1} cm^{-2}, FE of nearly 100% under concentration of 10 mM), the catalyst with S-L junction succeeded in removing NO_3^- to low level within 3 h, while the counterpart without the junction cannot meet the level after treatment of 48 h. Considering the practicality of the utilization of the high-value-added ammonia product, we implement additional experimental efforts to show a near-unity efficiency by the conversion of NO_3^- to a high-purity NH_4Cl, aiming to achieve sustainable development.

Efficient anion accumulation on the reaction interface is crucial for a wide range of renewable electricity-driven reduction applications. Thus, the strategy we proposed holds promise for various electrochemical anion reduction reactions, including NO_3^-, NO_2^-, AsO_4^{3-}, and $Cr_2O_7^{2-}$, etc, inspiring innovative design for water treatment and remediation in an environmentally friendly way. Such investigations could illuminate avenues for both fundamental research and practical applications across various scientific domains, ranging from physics, chemistry to environmental sciences.

Methods
Chemicals

Sodium molybdate dehydrate ($Na_2MoO_4 \cdot 2H_2O$, ≥ 99.95%), thiourea (CH_4N_2S, ≥ 99%), silver nitrate ($AgNO_3$, ≥ 99.8%), hydroxylamine hydrochloride ($NH_2OH \cdot HCl$, ≥ 99.99%), hexadecyl trimethyl ammonium bromide ($C_{19}H_{42}BrN$, CTAB, ≥ 99%), sodium tungstate dihydrate ($Na_2WO_4 \cdot 2H_2O$, ≥ 99.5%), salicylic acid ($C_7H_6O_3$, ≥ 99%), trisodium citrate dihydrate ($Na_3C_6H_5O_7 \cdot 2H_2O$, ≥ 99%), sulfanilamide ($C_6H_8N_2O_2S$, ≥ 99.8%), p-dimethylaminobenzaldehyde ((CH_3)$_2NC_6H_4CHO$, PDAB, ≥ 98%), sodium nitroferricyanide (III) dihydrate ($Na_2Fe(CN)_5NO \cdot 2H_2O$, ≥ 99.98%), N-(1-Naphthyl) ethylenediamine dihydrochloride ($C_{12}H_{14}N_2 \cdot 2HCl$, ≥ 98%), potassium sulfate (K_2SO_4, ≥ 99%), potassium nitrate-^{15}N ($^{15}KNO_3$, ≥ 99%), dimethyl sulfoxide (C_2H_6SO, DMSO-$d6$, ≥ 99.9%), maleic acid ($C_4H_4O_4$, ≥ 99%), and ammonium chloride ($^{14}NH_4Cl$, ≥ 99.8%), ammonium-^{15}N chloride ($^{15}NH_4Cl$, ≥ 98.5%) were purchased from Aldrich Chemical Reagent Co., Ltd. Sodium hydroxide (NaOH, ≥ 96%), sodium hypochlorite (NaClO, analytical pure), hydrochloric acid (HCl, 38%), potassium nitrate (KNO_3, ≥ 99.999%), potassium nitrite (KNO_2, ≥ 97%), and ethanol (C_2H_6O, ≥ 99.7%) were purchased from Sinopharm Chemical Reagent Co., Ltd. All chemicals were used as received without further purification. The water used in this research was purified through a Millipore system.

Preparation of Ag-MoS2

For the synthesis of Ag-MoS_2 in a typical hydrothermal process, 4.27 mmol of $Na_2MoO_4 \cdot 2H_2O$, 18.40 mmol of CH_4N_2S, a certain amount of $AgNO_3$, and 10.43 mmol of $NH_2OH \cdot HCl$ were dissolved in 50 mL of deionized water under vigorous stirring for 0.5 h. 0.18 g of CTAB was then added to the mixed solution, and the pH value of the mixture was adjusted to 6. After that, carbon cloth with an area of 4×4 cm^2 and a thickness of 0.35 mm was immersed into the homogeneous solution. The mixture was subsequently transferred into a 100 mL Teflon-lined stainless-steel autoclave and heated at 180 °C for 24 h in an oven. After cooling down to room temperature naturally, the products were washed with ethanol and deionized (DI) water repeatedly, followed by vacuum-freeze drying. The obtained sample was Ag-MoS_2 grown on carbon cloth (catalyst mass of ~ 5 mg cm^{-2}). Ag-MoS_2 catalysts with various Ag-doped amounts were prepared according to the above procedure by changing the additional amount of $AgNO_3$. Specifically, 0.213 mmol, 0.426 mmol, 0.639 mmol and 0.852 mmol $AgNO_3$ were added to achieve 1.87 wt%, 3.49 wt%, 5.91 wt% and 6.91 wt% Ag doping amounts, respectively. These catalysts were denoted as Ag-MoS_2-5, Ag-MoS_2-10, Ag-MoS_2-15 and Ag-MoS_2-20 (Supplementary Table S1).

Preparation of MoS2

In a typical synthesis of MoS_2, 4.27 mmol of $Na_2MoO_4 \cdot 2H_2O$, 18.40 mmol of CH_4N_2S, and 10.43 mmol of $NH_2OH \cdot HCl$ were dissolved in 50 mL of deionized water under vigorous stirring for 0.5 h. 0.18 g CTAB was then added to the mixed solution, and the pH value of the mixture was adjusted to 6. After that, carbon cloth with an area of 4×4 cm^2 and a thickness of 0.35 mm was immersed into the homogeneous solution. The mixture was subsequently transferred into a 100 mL Teflon-lined stainless-steel autoclave and heated at 180 °C for 24 h in an oven. After cooling down to room temperature naturally, the products were washed with ethanol and DI water repeatedly, followed by vacuum-freeze drying. The obtained sample was MoS_2 grown on carbon cloth (catalyst mass of ~ 5 mg cm^{-2}).

Preparation of W-MoS2

To systhesize W-MoS_2, 4.27 mmol of $Na_2MoO_4 \cdot 2H_2O$, 18.40 mmol of CH_4N_2S, 0.426 mmol of $Na_2WO_4 \cdot 2H_2O$, and 10.43 mmol of $NH_2OH \cdot HCl$ were dissolved in 50 mL of deionized water under vigorous stirring for 0.5 h. 0.18 g of CTAB was then added to the mixed solution, and the pH value of the mixture was adjusted to 6. After that, carbon cloth with an area of 4×4 cm^2 and a thickness of 0.35 mm was immersed into the homogeneous solution. The mixture was subsequently transferred into a 100 mL Teflon-lined stainless-steel autoclave and heated at 180 °C for 24 h in an oven. After cooling down to room temperature naturally, the products were washed with ethanol and DI water repeatedly, followed by vacuum-freeze drying. The obtained sample was W-MoS_2 grown on carbon cloth (catalyst mass of ~ 5 mg cm^{-2}).

Electrochemical testing

Before the NO_3RR tests, the pretreatment of Nafion 117 membrane (area: a circular shape with a diameter of 2 cm and a thickness of ~ 183 μm) was as follows: the membrane was first oxidized in 5% H_2O_2 solution at 80 °C for 1 h, next boiled in DI water for 1 h, then used 0.5 M H_2SO_4 at 80 °C for 1 h, finally washed with DI water.

The NO_3RR tests were performed on an electrochemical workstation (PARSTAT 4000) with a typical three-electrode flow cell, including as-prepared catalyst electrode (area of 1×1 cm^2, catalyst mass of ~ 5 mg cm^{-2}), IrO_2 electrode (area of 1×1 cm^2), and a saturated calomel electrode as the working electrode, counter electrode, and reference electrode, respectively. Nafion 117 membrane was used to separate the anodic cell and cathodic cell. The flow rate of electrolyte (0.5 M K_2SO_4 with 10 mM NO_3^-) was set at 2 mL min^{-1} in cathodic and anodic chambers. All potentials reported in this work were referred to the RHE scale via calibration by the following equation: E(versus RHE) = E(versus SCE) + 0.244 + 0.0591 × pHvalue. The three

batches of catalysts (Ag-MoS$_2$ (AgNO$_3$ amount of 0.426 mmol), MoS$_2$ and W-MoS$_2$) were synthesized, respectively, and their NO$_3$RR performance at various potentials were tested. The error bars were the mean values standard deviation according to the obtained data. For the chronoamperometry measurement, the potential was applied from −0.2 to −1.0 versus RHE. LSV was carried out in a voltage window from 0.25 to −1.65 V versus RHE at scan rates of 10 mV·s^{-1}. EIS of the samples was performed at the frequency region from 10^6 to 10^{-2} Hz with an amplitude of 20 mV at various applied potentials. During the electrochemical testing process, no iR compensation was performed. Mott-Schottky measurements were carried out at the frequency of 1000 Hz under dark conditions to obtain the flat band potential and carrier concentration of the samples, in which the dielectric constant of MoS$_2$ was 7.6[75,84].

Detection and quantification of NH$_3$ using UV-vis

The concentration of NH$_3$ after chronoamperometry measurements with different potentials was detected by the salicylic acid method[85]. The cathodic electrolyte after electrolysis was collected and diluted to the detection range. Then, 2 mL of diluted liquid was added to 2 mL of 1 M NaOH solution containing 5 wt% C$_7$H$_6$O$_3$ and 5 wt% Na$_3$C$_6$H$_5$O$_7$·2H$_2$O. 1 mL of 0.05 M NaClO and 0.2 mL of C$_5$FeN$_6$Na$_2$O solution (1 wt%) were subsequently mixed with the aforementioned solution and shaken well. After standing for 2 h, UV-vis spectrophotometer measurements were performed with the range from 500 to 800 nm, and the absorbance value at the wavelength of 655 nm was recorded. The concentration-absorbance curve was calibrated using standard ammonium chloride solution with concentrations of 0.5, 1.0, 3.0, 5.0, 10.0, 20.0 and 30.0 µg mL^{-1} in 0.5 M K$_2$SO$_4$ with NO$_3^-$. The fitting curve ($y = 0.10x + 0.01$, $R^2 = 0.999$) exhibited a good linear relation of absorbance value with NH$_4^+$ concentration.

Detection and quantification of NO$_3^-$ using UV-vis

The cathodic electrolyte after electrolysis was collected and diluted to the detection range. In the process, 5 mL of diluted sample solution was mixed with 0.1 mL of 1 M HCl. After standing for 20 min, the UV-vis absorbance at the wavelength ranging from 215 to 280 nm was recorded[86,87]. The absorbance difference between the wavelengths at 220 and 275 nm was calculated using the equation: A = A$_{220 nm}$ − A$_{275 nm}$. The concentration-absorbance difference curve was calibrated using standard KNO$_3$ solution with 1, 5, 10, 20, 30 and 50 µg mL^{-1} concentrations. The fitting curve ($y = 0.034x − 0.036$, $R^2 = 0.999$) exhibited a good linear relation of absorbance value with NO$_3^-$ concentration.

Detection and quantification of NO$_2^-$ using UV-vis

The preparation of the color reagent was as follows[86,87]: First, 0.5 g of C$_6$H$_8$N$_2$O$_2$S was dissolved in 50 mL of 2.0 M HCl solution, which was labeled as reagent A. 20 mg of N-(1-naphthyl) ethylenediamine dihydrochloride was then dispersed in 20 mL of DI water, which was labeled as reagent B. After 0.1 mL of reagent A mixed with 5 mL of standard or diluted sample solutions, 0.1 mL of reagent B was finally injected into the homogeneous solution, shaking up and standing for 30 min. The UV-vis absorbance at the wavelength ranging from 400 to 640 nm was recorded, in which the characteristic absorption peak of NO$_2^-$ was identified at 540 nm. The concentration-absorbance difference curve was calibrated using standard KNO$_2$ solution with concentrations of 0.2, 0.5, 1.0, and 2.0 µg mL^{-1}. The fitting curve ($y = 0.446x + 0.039$, $R^2 = 0.999$) exhibited a good linear relation of absorbance value with NO$_2^-$ concentration.

Detection and quantification of NH$_3$ using ^{1}H NMR

^{14}NO$_3^-$ and ^{15}NO$_3^-$ isotope labeling experiments were carried out on a Bruker AVANCE III HD NMR spectrometer (600 MHz) to support the UV-vis results[12]. After electrolysis, the pH value of the cathodic electrolyte was adjusted to 2 with 1 M HCl. 0.5 mL of the homogeneous

solution was then mixed with 0.1 mL DMSO-$d6$ with 0.04% C$_4$H$_4$O$_4$. ^{1}H NMR was recorded to quantitatively determine NH$_3$ concentration according to the corresponding standard curves.

Electrochemical in situ Raman spectroscopy.

In situ Raman spectroscopy was measured by inVia Reflex (Renishaw, UK) with a 532 nm laser as the excitation source[20]. The electrochemical process was performed in the three-electrode custom-made Teflon reactor with a quartz window, including Ag/AgCl, Pt wire, and catalysts coated on the Au electrode as the reference electrode, counter electrode, and working electrode, respectively. The spectra were recorded by the potential from OCP to −0.6 V versus RHE.

Electrochemical in situ ATR-IR spectroscopy.

ATR-IR spectroscopy was tested on a Nicolet iS50 FT-IR spectrometer equipped with an MCT detector and cooled by liquid nitrogen[20]. The electrochemical process was performed in the three-electrode custom-made reactor, including Ag/AgCl and Pt wire as the reference electrode and counter electrode, respectively. The working electrode was prepared as follows: The Si semi-cylindrical prism was first polished with Al$_2$O$_3$ powder and sonicated in acetone and deionized water. The Si was placed in a piranha solution at 60 °C for 20 min to remove the organic contaminants. Then the reflecting surface of Si was deposited in the Au precursor mixture at 60 °C for 10 min, and the Au-coated Si conductive substrate was obtained. The catalyst ink was finally coated on the substrate-reflecting surface. After that, the spectra were recorded by the potential from 0.4 V to −1.0 V versus RHE. The spectrum collected at OCP was as background subtraction.

Electrochemical online DEMS tests.

The online DEMS tests[21] were measured in the three-electrode customized reactors containing 0.5 M K$_2$SO$_4$ with 10 mM NO$_3^-$ electrolyte, including catalysts coated on breathable film with Au plating layer, Pt wire, and saturated Ag/AgCl electrode as the working electrode, the counter electrode and the reference electrode, respectively. The potential of OCP and −0.6 V versus RHE were applied alternately with an interval of 3 min after the baseline of the mass spectrometry kept steady. During the electrochemical process, the differential mass signals were recorded when the gaseous products formed on the electrode surface. The operation process was repeated five cycles to avoid accidental errors.

Direct ammonia product synthesis.

By coupling NO$_3$RR with the Ar stripping process, the cathodic electrolyte after electrolysis was adjusted to alkaline state, and sealed in a conical flask at 70 °C with flowing 100 sccm Ar gas to purge the NH$_3$ gas out. The outlet stream was injected into 2 M HCl to capture the NH$_3$ product. The NH$_3$ amount in all the solutions was evaluated by the salicylic acid method mentioned above, and the removal efficiency and collection efficiency were calculated as following equations[12], respectively:

$$\text{Removed NH}_3 \text{ via Ar stripping} = 1 - \frac{\text{NH}_3 \text{ left after Ar stripping (mol)}}{\text{initial NH}_3 \text{ (mol)}} \tag{1}$$

$$\text{Acid collected NH}_3 = \frac{\text{NH}_3 \text{ in acid trap (mol)}}{\text{removed NH}_3 \text{ via Ar stripping (mol)}} \tag{2}$$

To estimate the efficiency of the NH$_4$Cl product, the HCl solution with the trapped NH$_3$ was dried by rotary evaporator at 70 °C. The generated NH$_4$Cl was measured by a balance and analyzed by XRD. The collection efficiency of NH$_4$Cl from the acid trap was calculated by the

following equation:

$$\text{Collected NH}_4\text{Cl from acid trap} = \frac{\text{collected dried out NH}_4\text{Cl (mol)}}{\text{acid collected NH}_3 \text{ (mol)}}$$

$$(3)$$

DFT calculations. All calculations were carried out by spin-polarized DFT with the Vienna Ab initio Simulation Package (VASP)[88,89]. Electron exchange-correlation was expressed by the Perdew-Burke-Ernzerhof (PBE) functional within the generalized gradient approximation (GGA)[90]. To describe the ionic cores, the projector augmented wave (PAW) pseudopotential was applied[91,92]. The plane wave energy cutoff, and convergence criterion for electronic energy and forces were set as 450 eV, 10^{-5} eV, and 0.02 eV/Å. van der Waals (VDW) interactions were corrected using the D3 method of Grimme[93]. To compare the electronic structures of MoS_2, Ag-MoS_2 and W-MoS_2, we constructed a $2 \times 2 \times 2$ MoS_2 supercell containing 16 Mo atoms and 32 S atoms. Substituting one Mo atom with an Ag atom is referred to as Ag-MoS_2, while substituting one MoS_2 atom with a W atom is referred to as W-MoS_2. For investigating the reaction pathways of nitrate ions on three catalytic surfaces, we built a nanoribbon containing 20 Mo atoms and 40 S atoms. The bottom two layers were fixed to simulate the edge of a single-layer MoS_2. For Ag-MoS_2 and W-MoS_2, we replaced one edge Mo atom with an Ag atom and a W atom, respectively. To avoid periodic interlayer interactions, we introduced a vacuum layer of 20 Å in the Z and Y directions. Aqueous phase H_2O and NO_3^- were as the energetics references.

Data availability

Full data supporting the findings of this study are available within the article and its Supplementary Information, as well as from the corresponding author upon reasonable request. Source data are provided in this paper.

References

1. Chen, J. G. et al. Beyond fossil fuel-driven nitrogen transformations. *Science* **360**, eaar6611 (2018).
2. Chang, F., Gao, W., Guo, J. & Chen, P. Emerging materials and methods toward ammonia-based energy storage and conversion. *Adv. Mater.* **33**, e2005721 (2021).
3. Guo, J. & Chen, P. Catalyst: NH₃ as an energy carrier. *Chem* **3**, 709–712 (2017).
4. Chatterjee, S., Parsapur, R. K. & Huang, K.-W. Limitations of ammonia as a hydrogen energy carrier for the transportation sector. *ACS Energy Lett.* **6**, 4390–4394 (2021).
5. Kitano, M. et al. Ammonia synthesis using a stable electride as an electron donor and reversible hydrogen store. *Nat. Chem.* **4**, 934–940 (2012).
6. Han, G.-F. et al. Mechanochemistry for ammonia synthesis under mild conditions. *Nat. Nanotechnol.* **16**, 325–330 (2021).
7. Service, R. F. New recipe produces ammonia from air, water, and sunlight. *Science* **345**, 610 (2014).
8. Kyriakou, V., Garagounis, I., Vourros, A., Vasileiou, E. & Stoukides, M. An electrochemical Haber-Bosch process. *Joule* **4**, 142–158 (2020).
9. John, J., MacFarlane, D. R. & Simonov, A. N. The why and how of NOₓ electroreduction to ammonia. *Nat. Catal.* **6**, 1125–1130 (2023).
10. Chen, F.-Y. et al. Electrochemical nitrate reduction to ammonia with cation shuttling in a solid electrolyte reactor. *Nat. Catal.* **7**, 1032–1043 (2024).
11. Fang, J.-Y. et al. Ampere-level current density ammonia electrochemical synthesis using CuCo nanosheets simulating nitrite reductase bifunctional nature. *Nat. Commun.* **13**, 7899 (2022).
12. Chen, F. Y. et al. Efficient conversion of low-concentration nitrate sources into ammonia on a Ru-dispersed Cu nanowire electrocatalyst. *Nat. Nanotechnol.* **17**, 759–767 (2022).
13. Liao, W. et al. Boosting nitrogen activation via Ag nanoneedle arrays for efficient ammonia synthesis. *ACS Nano* **17**, 411–420 (2023).
14. Liao, W. et al. Interfacial engineering promoting electrosynthesis of ammonia over Mo/phosphotungstic acid with high performance. *Adv. Funct. Mater.* **31**, 2009151 (2021).
15. Liao, W. et al. Triggering in-plane defect cluster on MoS₂ for accelerated dinitrogen electroreduction to ammonia. *J. Energy Chem.* **62**, 359–366 (2021).
16. Suryanto, B. H. R. et al. Nitrogen reduction to ammonia at high efficiency and rates based on a phosphonium proton shuttle. *Science* **372**, 1187–1191 (2021).
17. Du, H.-L. et al. Electroreduction of nitrogen with almost 100% current-to-ammonia efficiency. *Nature* **609**, 722–727 (2022).
18. Li, K. et al. Enhancement of lithium-mediated ammonia synthesis by addition of oxygen. *Science* **374**, 1593–1597 (2021).
19. Fu, X. et al. Continuous-flow electrosynthesis of ammonia by nitrogen reduction and hydrogen oxidation. *Science* **379**, 707–712 (2023).
20. Liao, W. et al. Sustainable conversion of alkaline nitrate to ammonia at activities greater than 2 A cm⁻². *Nat. Commun.* **15**, 1264 (2024).
21. Han, S. et al. Ultralow overpotential nitrate reduction to ammonia via a three-step relay mechanism. *Nat. Catal.* **6**, 402–414 (2023).
22. Wang, K. et al. Intentional corrosion-induced reconstruction of defective NiFe layered double hydroxide boosts electrocatalytic nitrate reduction to ammonia. *Nat. Water* **1**, 1068–1078 (2023).
23. Daiyan, R. et al. Nitrate reduction to ammonium: From CuO defect engineering to waste NOₓ-to-NH₃ economic feasibility. *Energ. Environ. Sci.* **14**, 3588–3598 (2021).
24. Yang, X. et al. Achievements, challenges, and perspectives on nitrogen electrochemistry for carbon-neutral energy technologies. *Angew. Chem. Int. Ed.* **62**, e202215938 (2023).
25. Burow, K. R., Nolan, B. T., Rupert, M. G. & Dubrovsky, N. M. Nitrate in groundwater of the united states, 1991–2003. *Environ. Sci. Technol.* **44**, 4988–4997 (2010).
26. Smolders, A. J. P., Lucassen, E. C. H. E. T., Bobbink, R., Roelofs, J. G. M. & Lamers, L. P. M. How nitrate leaching from agricultural lands provokes phosphate eutrophication in groundwater fed wetlands: The sulphur bridge. *Biogeochemistry* **98**, 1–7 (2009).
27. Ren, Y. et al. Microscopic-level insights into the mechanism of enhanced NH₃ synthesis in plasma-enabled cascade N₂ oxidation–electroreduction system. *J. Am. Chem. Soc.* **144**, 10193–10200 (2022).
28. Sun, J. et al. Sustainable ammonia production via nanosecond-pulsed plasma oxidation and electrocatalytic reduction. *Appl. Catal. B-Environ.* **342**, 123426 (2024).
29. Liu, H. et al. Efficient electrochemical nitrate reduction to ammonia with copper-supported rhodium cluster and single-atom catalysts. *Angew. Chem. Int. Ed.* **61**, e202202556 (2022).
30. Gao, W. et al. Alloying of Cu with Ru enabling the relay catalysis for reduction of nitrate to ammonia. *Adv. Mater.* **35**, 2202952 (2023).
31. Xie, M. et al. Intermetallic single-atom alloy In-Pd bimetallene for neutral electrosynthesis of ammonia from nitrate. *J. Am. Chem. Soc.* **145**, 13957–13967 (2023).
32. Song, Z. et al. Efficient electroreduction of nitrate into ammonia at ultralow concentrations via an enrichment effect. *Adv. Mater.* **34**, e2204306 (2022).
33. Zhang, S., Li, M., Li, J., Song, Q. & Liu, X. High-ammonia selective metal–organic framework–derived Co-doped Fe/Fe₂O₃ catalysts for electrochemical nitrate reduction. *PNAS* **119**, e2115504119 (2022).
34. Chen, G.-F. et al. Electrochemical reduction of nitrate to ammonia via direct eight-electron transfer using a copper–molecular solid catalyst. *Nat. Energy* **5**, 605–613 (2020).
35. Van Langevelde, P. H., Katsounaros, I. & Koper, M. T. M. Electrocatalytic nitrate reduction for sustainable ammonia production. *Joule* **5**, 290–294 (2021).

36. Huang, Y. et al. Pulsed electroreduction of low-concentration nitrate to ammonia. *Nat. Commun.* **14**, 7368 (2023).

37. Su, L. et al. Electrochemical nitrate reduction by using a novel Co_3O_4/Ti cathode. *Water Res.* **120**, 1–11 (2017).

38. Chauhan, R. & Srivastava, V. C. Electrochemical denitrification of highly contaminated actual nitrate wastewater by Ti/RuO_2 anode and iron cathode. *Chem. Eng. J.* **386**, 122065 (2020).

39. Paredes, I., Otero, N., Soler, A., Green, A. J. & Soto, D. X. Agricultural and urban delivered nitrate pollution input to mediterranean temporary freshwaters. *Agr. Ecosyst. Environ.* **294**, 106859 (2020).

40. Lee, C.-M. et al. Contribution of nitrate-nitrogen concentration in groundwater to stream water in an agricultural head watershed. *Environ. Res.* **184**, 109313 (2020).

41. Sun, W. J. et al. Built-in electric field triggered interfacial accumulation effect for efficient nitrate removal at ultra-low concentration and electroreduction to ammonia. *Angew. Chem. Int. Ed.* **60**, 22933–22939 (2021).

42. Luo, H. et al. Modulating the active hydrogen adsorption on Fe—N interface for boosted electrocatalytic nitrate reduction with ultra-long stability. *Adv. Mater.* **35**, 2304695 (2023).

43. Hou, Y., Li, T., Yan, S. & Zou, Z. Oriented-growth Ta_3N_5/$SrTaO_2N$ array heterojunction with extended depletion region for improved water oxidation. *Appl. Catal. B-Environ.* **269**, 118777 (2020).

44. Ding, C., Shi, J., Wang, Z. & Li, C. Photoelectrocatalytic water splitting: Significance of cocatalysts, electrolyte, and interfaces. *ACS Catal.* **7**, 675–688 (2016).

45. Niu, H. et al. Structurally stable ultrathin 1T-2H MoS_2 heterostructures coaxially aligned on carbon nanofibers toward superhigh-energy-density supercapacitor and enhanced electrocatalysis. *Chem. Eng. J.* **399**, 125672 (2020).

46. Liu, R. et al. Highly efficient electrocatalytic N_2 reduction to ammonia over metallic 1T phase of MoS_2 enabled by active sites separation mechanism. *Adv. Sci.* **9**, 2103583 (2021).

47. Xu, T. N. et al. Realization of Ag-S codoped p-type ZnO thin films. *Appl. Surf. Sci.* **316**, 62–65 (2014).

48. Lim, J. W., Dong, W. J., Cho, W. S., Yoo, C. J. & Lee, J.-L. CuS_x catalysts by Ag-mediated corrosion of Cu for electrochemical reduction of sulfur-containing CO_2 gas to HCOOH. *ACS Catal.* **12**, 13174–13185 (2022).

49. Xuan, N. et al. Single-atom electroplating on two dimensional materials. *Chem. Mater.* **31**, 429–435 (2019).

50. Du, M. H., Yan, J., Cooper, V. R. & Eisenbach, M. Tuning fermi levels in intrinsic antiferromagnetic topological insulators $MnBi_2Te_4$ and $MnBi_4Te_7$ by defect engineering and chemical doping. *Adv. Funct. Mater.* **31**, 2006516 (2020).

51. Li, M. et al. Controllable p-type doping of monolayer MoS_2 with tantalum by one-step chemical vapor deposition. *J. Mater. Chem. C.* **10**, 7662–7673 (2022).

52. Lu, X., Song, H., Cai, J. & Lu, S. Recent development of electrochemical nitrate reduction to ammonia: A mini review. *Electrochem. Commun.* **129**, 107094 (2021).

53. Zhang, X. et al. Recent advances in non-noble metal electrocatalysts for nitrate reduction. *Chem. Eng. J.* **403**, 126269 (2021).

54. Koval, C. A. & Howard, J. N. Electron transfer at semiconductor electrode-liquid electrolyte interfaces. *Chem. Rev.* **92**, 411–433 (1992).

55. Mao, S. et al. Specific adsorption-oxidation strategy in cathode inner helmholtz plane enabling 4.6 V practical lithium-ion full cells. *Nano Lett.* **23**, 7014–7022 (2023).

56. Wang, L., Shen, C., Huang, C., Chen, J. & Zheng, J. Regulating the electrical double layer with supramolecular cyclodextrin anions for dendrite-free zinc electrodeposition. *ACS Nano* **17**, 24619–24631 (2023).

57. Yan, C. et al. Regulating the inner helmholtz plane for stable solid electrolyte interphase on lithium metal anodes. *J. Am. Chem. Soc.* **141**, 9422–9429 (2019).

58. Luo, J. et al. Regulating the inner helmholtz plane with a high donor additive for efficient anode reversibility in aqueous Zn-ion. *batteries.* *Angew. Chem. Int. Ed.* **135**, e202302302 (2023).

59. Herzog, G., Moujahid, W., Strutwolf, J. & Arrigan, D. W. M. Interactions of proteins with small ionised molecules: Electrochemical adsorption and facilitated ion transfer voltammetry of haemoglobin at the liquid|liquid interface. *Analyst* **134**, 1608–1613 (2009).

60. Luo, J. et al. Regulating the inner helmholtz plane with a high donor additive for efficient anode reversibility in aqueous Zn-ion batteries. *Angew. Chem. Int. Ed.* **62**, e202302302 (2023).

61. Luo, Z.-Z. et al. Extraordinary role of Zn in enhancing thermoelectric performance of Ga-doped n-type PbTe. *Energ. Environ. Sci.* **15**, 368–375 (2022).

62. Li, C.-Y. et al. In situ probing electrified interfacial water structures at atomically flat surfaces. *Nat. Mater.* **18**, 697–701 (2019).

63. Cai, C. et al. Atomically local electric field induced interface water reorientation for alkaline hydrogen evolution reaction. *Angew. Chem. Int. Ed.* **62**, e202300873 (2023).

64. Wang, Y. H. et al. In situ Raman spectroscopy reveals the structure and dissociation of interfacial water. *Nature* **600**, 81–85 (2021).

65. Zhao, R. et al. A Bi-Co corridor construction effectively improving the selectivity of electrocatalytic nitrate reduction toward ammonia by nearly 100%. *Adv. Mater.* **35**, 2306633 (2023).

66. Kumar, A. et al. Efficient nitrate conversion to ammonia on f-block single-atom/metal oxide heterostructure via local electron-deficiency modulation. *ACS Nano* **16**, 15297–15309 (2022).

67. Yang, C. et al. Large-scale synthetic Mo@(2H-1T)-$MoSe_2$ monolithic electrode for efficient hydrogen evolution in all pH scale ranges and seawater. *Appl. Catal. B Environ.* **304**, 120993 (2022).

68. Chen, W. et al. Deciphering the alternating synergy between interlayer Pt single-atom and NiFe layered double hydroxide for overall water splitting. *Energ. Environ. Sci.* **14**, 6428–6440 (2021).

69. Bu, L. et al. Photolysis of nitrate by solar light in agricultural runoffs: Degradation of emerging contaminant *vs.* Formation of unintended products. *Sep. Purif. Technol.* **269**, 118751 (2021).

70. Andersen, S. Z. et al. A rigorous electrochemical ammonia synthesis protocol with quantitative isotope measurements. *Nature* **570**, 504–508 (2019).

71. Wang, Y. et al. Structurally disordered RuO_2 nanosheets with rich oxygen vacancies for enhanced nitrate electroreduction to ammonia. *Angew. Chem. Int. Ed.* **61**, e202202604 (2022).

72. Lim, J. et al. Structure sensitivity of Pd facets for enhanced electrochemical nitrate reduction to ammonia. *ACS Catal.* **11**, 7568–7577 (2021).

73. Liao, P. H., Chen, A. & Lo, K. V. Removal of nitrogen from swine manure wastewaters by ammonia stripping. *Bioresour. Technol.* **54**, 17–20 (1995).

74. Yuan, M.-H., Chen, Y.-H., Tsai, J.-Y. & Chang, C.-Y. Ammonia removal from ammonia-rich wastewater by air stripping using a rotating packed bed. *Process Saf. Environ. Prot.* **102**, 777–785 (2016).

75. Zhang, G. et al. Ammonia recovery from nitrate-rich wastewater using a membrane-free electrochemical system. *Nat. Sustain.* **7**, 1251–1263 (2024).

76. Fan, K. et al. Active hydrogen boosts electrochemical nitrate reduction to ammonia. *Nat. Commun.* **13**, 7958 (2022).

77. Wirz, R., Ferri, D. & Baiker, A. ATR-IR spectroscopy of pendant NH_2 groups on silica involved in the knoevenagel condensation. *Langmuir* **22**, 3698–3706 (2006).

78. Wiles, D. M. & Suprunchuk, T. The infrared absorption spectra of thiosemicarbazide and related compounds: NH_2 and NH vibrations. *Can. J. Chem.* **47**, 1087–1089 (1969).

79. Milligan, D. E. & Jacox, M. E. Matrix-isolation infrared spectrum of the free radical NH_2. *J. Chem. Phys.* **43**, 4487–4493 (1965).

80. Gong, Z. et al. Modulating metal-nitrogen coupling in anti-perovskite nitride via cation doping for efficient reduction of nitrate to ammonia. *Angew. Chem. Int. Ed.* **135**, e202308775 (2023).

81. Chen, L., Li, J. & Ge, M. Drift study on cerium–tungsten/titiania catalyst for selective catalytic reduction of NO_x with NH_3. *Environ. Sci. Technol.* **44**, 9590–9596 (2010).

82. Böker, T. et al. Band structure of MoS_2, $MoSe_2$, and $\alpha–MoTe_2$: Angle-resolved photoelectron spectroscopy and ab initio calculations. *Phys. Rev. B* **64**, 235305 (2001).

83. Alidoust, N. et al. Observation of monolayer valence band spin-orbit effect and induced quantum well states in MoX_2. *Nat. Commun.* **5**, 4673 (2014).

84. Evans, B. L., Young, P. A. & Ditchburn, R. W. Optical absorption and dispersion in molybdenum disulphide. *Proc. R. Soc. Lond. Ser. A* **284**, 402–422 (1997).

85. Searle, P. L. The berthelot or indophenol reaction and its use in the analytical chemistry of nitrogen. *Analyst* **109**, 549–568 (1984).

86. Carvalho, A. P., Meireles, L. A. & Malcata, F. X. Rapid spectro-photometric determination of nitrates and nitrites in marine aqueous culture media. *Analusis* **26**, 347–351 (1998).

87. Polatides, C. & Kyriacou, G. Electrochemical reduction of nitrate ion on various cathodes – reaction kinetics on bronze cathode. *J. Appl. Electrochem.* **35**, 421–427 (2005).

88. Kresse, G. & Furthmüller, J. Efficiency of ab-initio total energy calculations for metals and semiconductors using a plane-wave basis set. *Comp. Mater. Sci.* **6**, 15–50 (1996).

89. Kresse, G. & Furthmüller, J. Efficient iterative schemes for ab initio total-energy calculations using a plane-wave basis set. *Phys. Rev. B* **54**, 11169–11186 (1996).

90. Perdew, J. P., Burke, K. & Ernzerhof, M. Generalized gradient approximation made simple. *Phys. Rev. Lett.* **77**, 3865–3868 (1996).

91. Kresse, G. & Joubert, D. From ultrasoft pseudopotentials to the projector augmented-wave method. *Phys. Rev. B* **59**, 1758–1775 (1999).

92. Blöchl, P. E. Projector augmented-wave method. *Phys. Rev. B* **50**, 17953–17979 (1994).

93. Grimme, S., Antony, J., Ehrlich, S. & Krieg, H. A consistent and accurate ab initio parametrization of density functional dispersion correction (DFT-D) for the 94 elements H-Pu. *J. Chem. Phys.* **132**, 154104 (2010).

Acknowledgements

Author contributions

W.L., J.W., and M.L. conceived the research and supervised the project. W.L. and J.W. performed the experiments. W.L., J.W., M.L., X.Z., Q.W., C.K., T.C., H.L., Y.Z., C.C., J.F., L.Z., L.C., and B.X. analyzed the data. Y.T. and K.L. carried out the DFT simulations. W.L., J.W., C.L., and E.C. wrote the draft. All authors discussed the results and contributed to the writing of the manuscript.

Funding

Competing interests

The authors declare no competing interests.

Additional information

Supplementary information The online version contains supplementary material available at https://doi.org/10.1038/s41467-025-60671-y.

Correspondence and requests for materials should be addressed to Beidou Xi, Emiliano Cortés or Min Liu.

Peer review information *Nature Communications* thanks the anonymous reviewers for their contribution to the peer review of this work. A peer review file is available.

Reprints and permissions information is available at http://www.nature.com/reprints

Publisher's note Springer Nature remains neutral with regard to jurisdictional claims in published maps and institutional affiliations.